Geophysical Research Letters

RESEARCH LETTER
10.1029/2019GL082944

Quenching of Equatorial Magnetosonic Waves by Substorm Proton Injections

Guyue Dai[1,2,3], Zhenpeng Su[1,2], Nigang Liu[1,2,3], Bin Wang[4], Huinan Zheng[1,2], Yuming Wang[1,2], and Shui Wang[1,2]

[1]Department of Geophysics and Planetary Sciences, University of Science and Technology of China, Hefei, China, [2]CAS Center for Excellence in Comparative Planetology, Hefei, China, [3]Mengcheng National Geophysical Observatory, School of Earth and Space Sciences, University of Science and Technology of China, Hefei, China, [4]Beijing Institute of Tracing and Telecommunications Technology, Beijing, China

Key Points:
- The enhanced thermal pressure of hot protons can distort the geomagnetic field configuration and the cold plasma density distribution
- The magnetosonic wave quenching region can emerge closely following the substorm injection front under both high- and low-density conditions
- The magnetosonic wave quenching region can extend over 2 hr in magnetic local time and 0.5 Earth radii in radial distance

Supporting Information:
- Supporting Information S1

Correspondence to:
Z. Su
szpe@mail.ustc.edu.cn

Citation:
Dai, G., Su, Z., Liu, N., Wang, B., Zheng, H., Wang, W., et al. (2019). Quenching of equatorial magnetosonic waves by substorm proton injections. *Geophysical Research Letters*, *46*, 6156–6167. https://doi.org/10.1029/2019GL082944

Received 20 MAR 2019
Accepted 15 MAY 2019
Accepted article online 23 MAY 2019
Published online 17 JUN 2019

Abstract Near equatorial (fast) magnetosonic waves, characterized by high magnetic compressibility, are whistler-mode emissions destabilized by proton shell/ring distributions. In the past, substorm proton injections are widely known to intensify magnetosonic waves in the inner magnetosphere. Here we report the unexpected observations by the Van Allen Probes of the magnetosonic wave quenching associated with the substorm proton injections under both high- and low-density conditions. The enhanced proton thermal pressure distorted the background magnetic field configuration and the cold plasma density distribution. The reduced phase velocities locally allowed the weak growth or even damping of magnetosonic waves. Meanwhile, the spatially irregularly varying refractive indices might suppress the cumulative growth of magnetosonic waves. For intense injections, this wave quenching region could extend over 2 hr in magnetic local time and 0.5 Earth radii in radial distance. These results provide a new understanding of the generation and distribution of magnetosonic waves.

Plain Language Summary Magnetosonic waves are the near-equatorially confined electromagnetic emissions between the proton gyrofrequency and the lower hybrid frequency in the magnetosphere. Theoretical and observational studies have demonstrated the potential of the magnetosonic waves to accelerate the radiation belt electrons. It is therefore important to understand the generation process and the spatiotemporal distribution of the magnetosonic waves. The substorm activities injecting hot protons into the inner magnetosphere are conventionally considered to intensify the magnetosonic waves. By analyzing the wave and particle data of the Van Allen Probes, we find a magnetosonic wave quenching region related to the distortion of the background magnetic field configuration and the cold plasma density distribution closely following the substorm injection front. We propose two possible causes for this phenomenon: (1) local weak growth or even damping of the magnetosonic waves with the reduced phase velocities and (2) suppression of the magnetosonic wave cumulative growth in the disturbed medium. This new finding may help refine the modeling of the magnetosonic waves and then the radiation belt electrons.

1. Introduction

Magnetosonic waves, also referred to as fast magnetosonic waves and equatorial noise, are the whistler-mode emissions with high magnetic compressibility (typically the ratio of parallel power to total power $P_{B\|}/P_B > 0.8$) confined near the magnetospheric equator (Gurnett, 1976; Russell et al., 1970). Theoretical (Horne et al., 2007; Shprits, 2009) and observational (Li et al., 2016; Xiao et al., 2015; Yang et al., 2017) studies have demonstrated that the magnetosonic waves can locally accelerate the radiation belt electrons mirroring off the equator. Therefore, it is important to understand the generation and distribution of the magnetosonic waves.

The Bernstein mode instability of hot protons with a velocity ring distribution can destabilize the magnetosonic waves at the quasi-perpendicular normal angles (Boardsen et al., 1992; Curtis & Wu, 1979; Gary et al., 2010; Gulelmi et al., 1975; Horne et al., 2000; Liu et al., 2011; Min et al., 2018; Perraut et al., 1982). Near the source region, the magnetosonic waves are characterized as the emission lines along the proton gyrofrequency harmonics in the high-resolution frequency-time spectrograms (e.g., Balikhin et al., 2015;

Perraut et al., 1982). These waves have been observed to propagate over a broad range of radial distances and magnetic local times (e.g., Santolík et al., 2002; Su et al., 2017). The nonlinear interactions between locally generated and spatially propagating magnetosonic waves likely produce the magnetosonic harmonic falling and rising emission lines in the high-resolution frequency-time spectrograms (Liu et al., 2018a). Spatiotemporal distributions of the magnetosonic waves are controlled by both substorm activities (Boardsen et al., 2016; Ma et al., 2013; Meredith et al., 2008) and solar wind disturbances (Kim & Chen, 2016; Kim & Shprits, 2017). During substorms, hot protons are injected into the inner magnetosphere, and because of the energy-dependent drift, ~10 keV proton rings form primarily in the dayside sector (Chen et al., 2010; Thomsen et al., 2011). A stronger substorm tends to allow the magnetosonic waves with a larger amplitude over a broader region (Meredith et al., 2008). The solar wind dynamic pressure fluctuations can adiabatically change the hot proton fluxes, causing the disappearance or emergence of the magnetosonic waves (Liu et al., 2018b). Without intense substorm proton injections, the magnetosonic waves are observable primarily during the time period with the enhanced solar wind dynamic pressure (Liu et al., 2018b).

In this letter, we report surprising observations by the Van Allen Probes (Mauk et al., 2013) of the magnetosonic wave quenching promptly following the substorm proton injections under both high- and low-density conditions. The wave quenching phenomenon was not related to the sudden change in the solar wind dynamic pressure, different in nature from that studied by Liu et al. (2018b). Investigation of this unexpected phenomenon may bring new insights on the generation and distribution of the magnetosonic waves.

2. Data and Method

On 30 August 2012, the Van Allen Probes were launched into the highly elliptical, low inclination orbits (Mauk et al., 2013). Here we use the data from the Electric and Magnetic Field Instrument and Integrated Science (EMFISIS) suite (Kletzing et al., 2013), the Energetic particle, Composition, and Thermal plasma (ECT) suite (Spence et al., 2013), and the Radiation Belt Storm Probes Ion Composition Experiment (RBSPICE; Mitchell et al., 2013) on this mission. The Waveform Receiver of the EMFISIS Waves instrument provides the standard survey product of the wave spectral matrix in 65 logarithmically spaced bins between 2 Hz and 12 kHz with a cadence of 6 s. To obtain the high-resolution wave spectral matrices below 32 Hz, we apply the Fast Fourier Transform on the magnetic field vectors with a sampling rate of 64 Hz measured by the EMFISIS triaxial fluxgate magnetometer. We perform the singular value decomposition (Santolík et al., 2003) of the magnetic spectral matrix to estimate the wave vector direction and the ellipticity of wave polarization (Santolík et al., 2002). With the upper hybrid resonance frequency measured by the high-frequency receiver of the EMFISIS Waves instrument, we can determine the cold electron density (Kurth et al., 2014). The Helium Oxygen Proton Electron instrument (HOPE; Funsten et al., 2013) and the Magnetic Electron Ion Spectrometer (MagEIS; Blake et al., 2013) of the ECT suite collectively provide the electron fluxes at energies ~10–10^6 eV; the HOPE and RBSPICE instruments together measure the proton fluxes at energies ~1–10^6 eV.

With the measurements mentioned above, we analyze the wave instability using our previously developed code (Liu et al., 2018b; Su et al., 2018) in the framework of the quasi-linear theory (Chen et al., 2010; Kennel, 1966). The wave convective growth rate is written as

$$K_i = -\frac{1}{|\mathbf{V}_{\mathrm{g}}|}\frac{D_{\mathrm{i}}}{\partial D^0/\partial\omega}, \tag{1}$$

with the real D^0 and the imaginary D_{i} parts of the determinant of plasma dispersion relation matrix, the wave angular frequency ω, and the group velocity V_{g}. D^0 is set to be the determinant of cold plasma wave dispersion relation matrix, and D_{i} depends on the derivatives of the hot particle phase space density with respect to pitch angle and energy (Chen et al., 2010, equations A3 and A4). To reduce data noises and gaps particularly at the low energies and the near-loss-cone pitch angles, we symmetrize the particle phase space densities with respect to the 90° pitch angle and then smooth them over ~5 min. At each energy channel, we use a smooth cubic spline (Reinsch, 1967) to approximate the pitch-angle distribution. For an arbitrary point in the pitch angle-energy space, we perform a two-dimensional B-spline interpolation (De Boor, 1977) to obtain the required derivatives of D_{i}. In this study, both the growth rates related to hot (0.1–200 keV) protons (Meredith et al., 2008) and the damping rates related to hot (0.1–200 keV) electrons (Horne et al., 2000) have been calculated and their differences are considered as the net growth rates of magnetosonic waves.

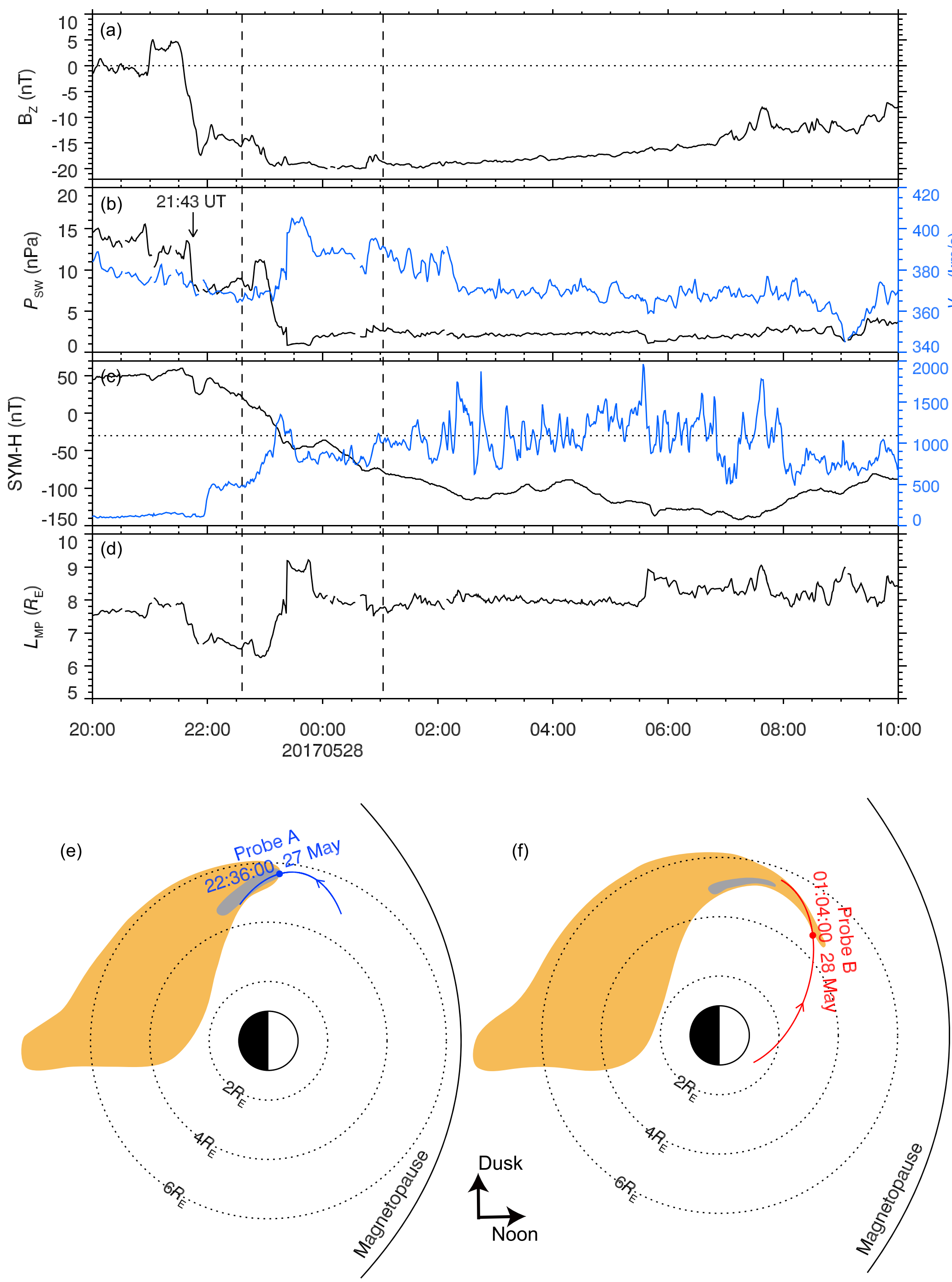

Figure 1. Interplanetary condition, geomagnetic indices and schematic diagrams for the 27-28 May 2017 event: (a) the southward interplanetary magnetic field B_Z; (b) the solar wind dynamic pressure P_{sw} (black) and flow velocity V_{sw} (blue); (c) geomagnetic indices SYM-H (black) and AE (blue); (d) subsolar magnetopause location L_{MP}; (e and f) schematic diagrams of magnetopause (black), substorm injection region (yellow), magnetosonic quenching region (gray), and Van Allen Probes trajectories (blue for Probe A and red for Probe B). In Figures 1a–1d, the two vertical dashed lines mark the injection times detected by the Van Allen Probes. In Figure 1b, the arrow marks the sudden decrease of the solar wind dynamic pressure.

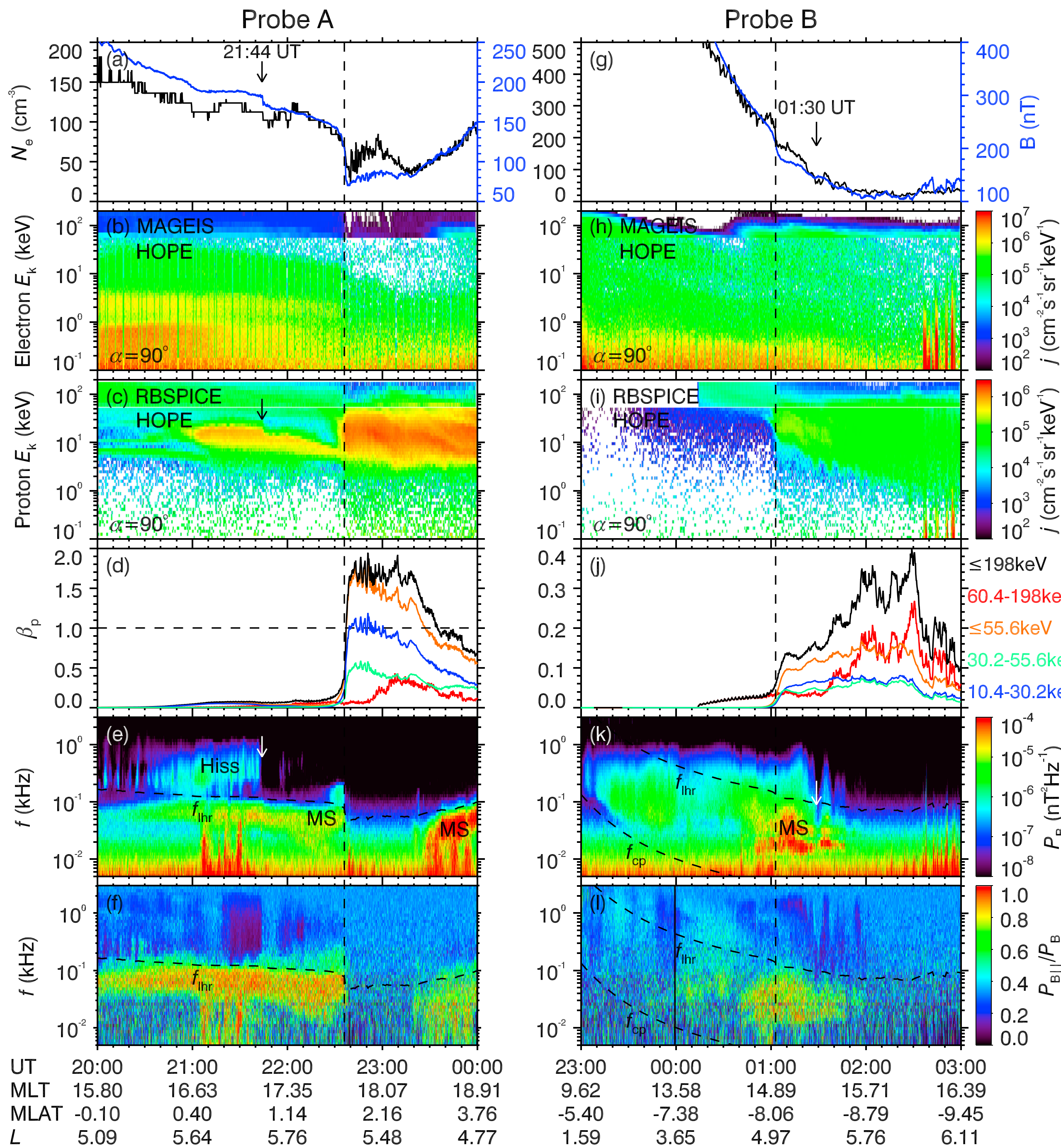

Figure 2. Evolution of magnetospheric environment during 27–28 May 2017: (a and g) cold electron density N_e (black) and magnetic field B (blue); (b and h) electron differential flux j at $\alpha = 90°$; (c and i) proton differential flux j at $\alpha = 90°$; (d and j) proton plasma beta β_p (color coded according to energy channel); (e and k) wave magnetic power spectral density P_B; (f and l) magnetic compressibility $P_{B||}/P_B$. The vertical dashed lines mark the injection fronts detected by the Van Allen Probes. The arrows in Figures 2a, 2c, and 2e denote the solar wind dynamic pressure reduction causing the magnetosoinc weakening and the hiss disappearance (Liu et al., 2017, 2018b). The arrows in Figures 2g and 2k denote the density slot without observable magnetosonic waves.

3. Magnetosonic Wave Quenching Under High-Density Condition

3.1. Event Overview

Figures 1 and 2 give an overview of the magnetosonic wave quenching event observed by the Van Allen Probes under the high-density condition during the 27–28 May 2017 geomagnetic storm (with the SYM-H minimum of −141 nT and the AE maximum of 1960 nT). This storm was triggered by an interplanetary magnetic cloud with the smoothly varying magnetic fields, and during the initial phase and the early main phase, the subsolar magnetopause had been compressed to $L_{\mathrm{MP}} \approx 6$ (Shue et al., 1998). Magnetosonic waves are identified as the electromagnetic emissions below the lower hybrid frequency f_{lhr}, with the high magnetic compressibility ($P_{\mathrm{B}\|}/P_{\mathrm{B}} > 0.8$).

From 20:00 to 24:00 UT on 27 May 2017, the Van Allen Probe A was located in the duskside (15 < MLT < 19) equatorial (|MLAT| < 4°) high-density region ($L \geq 4.77$ and $N_{\mathrm{e}} \geq 34\,\mathrm{cm}^{-3}$). Note that there was no clear plasmapause structure with a sharp density gradient and the observed densities (Figure S1 in the supporting information) were always beyond the typical values in the plasmatrough (Carpenter & Anderson, 1992; Sheeley et al., 2001). Before 21:10 UT, the magnetosonic waves were quite weak at a nearly constant frequency band (50–100 Hz), which were not generated locally but rather originated from the outer plasmasphere (Ma et al., 2014). The follow-up magnetosonic waves closely tracking f_{lhr} were most likely destabilized by the hot proton rings around 10 keV. At 21:44 UT (Figures 1d, 2a, 2c, 2e, and S2), the sudden decrease in the solar wind dynamic pressure caused the expansion of the magnetosphere, the adiabatic deceleration of hot protons, and then the slightly weakening of magnetosonic waves (Liu et al., 2018b). At 22:36 UT ($L = 5.64$, MLT = 17.77, and MLAT = 1.71°), there was a profound substorm-proton injection, leading to the enhancement of 1- to 100-keV proton fluxes by up to 2 orders of magnitude. Correspondingly, both the magnetic field strength and the cold electron density decreased and the magnetosonic waves were quenched. In the next 1 hr, although the Probe A went toward the Earth, the magnetic field magnitude and the cold electron density fluctuated around a low level. After 23:24 UT, intense magnetosonic waves occurred with the gradual increase of the magnetic field strength and the cold electron density.

This "trough" with a low level of magnetic field strength and the cold electron density was likely a result of the newly formed partial ring current during substorms (Daglis et al., 1999; Dessler & Karplus, 1961; Tsyganenko & Sitnov, 2005; Ukhorskiy et al., 2006; Xia et al., 2017). Following the previous studies (e.g., He et al., 2017; Xiong et al., 2017), we calculate the proton plasma beta β_{p} (the ratio of the thermal perpendicular pressure of hot protons to the magnetic pressure) to quantitatively describe the effect of the substorm proton injection on the magnetic field. The thermal pressure was mainly provided by the injected protons in the energy range of ≤55.6 keV, and the magnetic field strength decreased from 142 to 70 nT with the increase of β_{p} from 0.2 to 1.6. Under the magnetohydrodynamic frozen-in condition, the expansion of magnetic field lines would yield a decrease in the cold plasma density, explaining the high correlation between magnetic field magnitude and density after the substorm proton injection.

The Van Allen Probe B encountered this drifting substorm injection front at 01:04 UT ($L = 5.04$, MLT = 14.95 and MLAT = −8.11°) on 28 May 2017. Compared to the duskside observations by the Probe A, the injected proton fluxes observed by the Probe B in the afternoon sector were about three times weaker. Under the condition of $\beta_{\mathrm{p}} < 0.4$, the percent changes in the magnetic field and density were much weaker than those of the Probe A. And the magnetosonic waves were not quenched near the substorm injection front. After 01:45 UT, as the Probe B went far away from the equator (|MLAT|≥ 8.6°), the magnetosonic waves became unobservable.

3.2. Wave Instability and Propagation

In Figures 3 and 4, we analyze the linear instability of magnetosonic waves and their spatial propagation. As shown in Figures S3–S6, the observed particle distributions have been reasonably modeled. For the proton component, the wave growth rates near the nth harmonic of the proton gyrofrequency f_{cp} is proportional to a weighted integral (Boardsen et al., 1992; Chen et al., 2010; Schmidt, 1979)

$$K_{\mathrm{i}}(f)\big|_{f\approx nf_{\mathrm{cp}}} \propto \int_0^{\infty} J_n^2\left(\frac{k_\perp v_\perp}{2\pi f_{\mathrm{cp}}}\right) \left.\frac{\partial F(v_\|, v_\perp)}{\partial v_\perp}\right|_{v_\|=2\pi(f-nf_{\mathrm{cp}})/k_\|} dv_\perp, \tag{2}$$

with the proton phase space density $F(v_\|, v_\perp)$ in the velocity space, the parallel $k_\|$ and perpendicular $k_\perp$

10.1029/2019GL082944

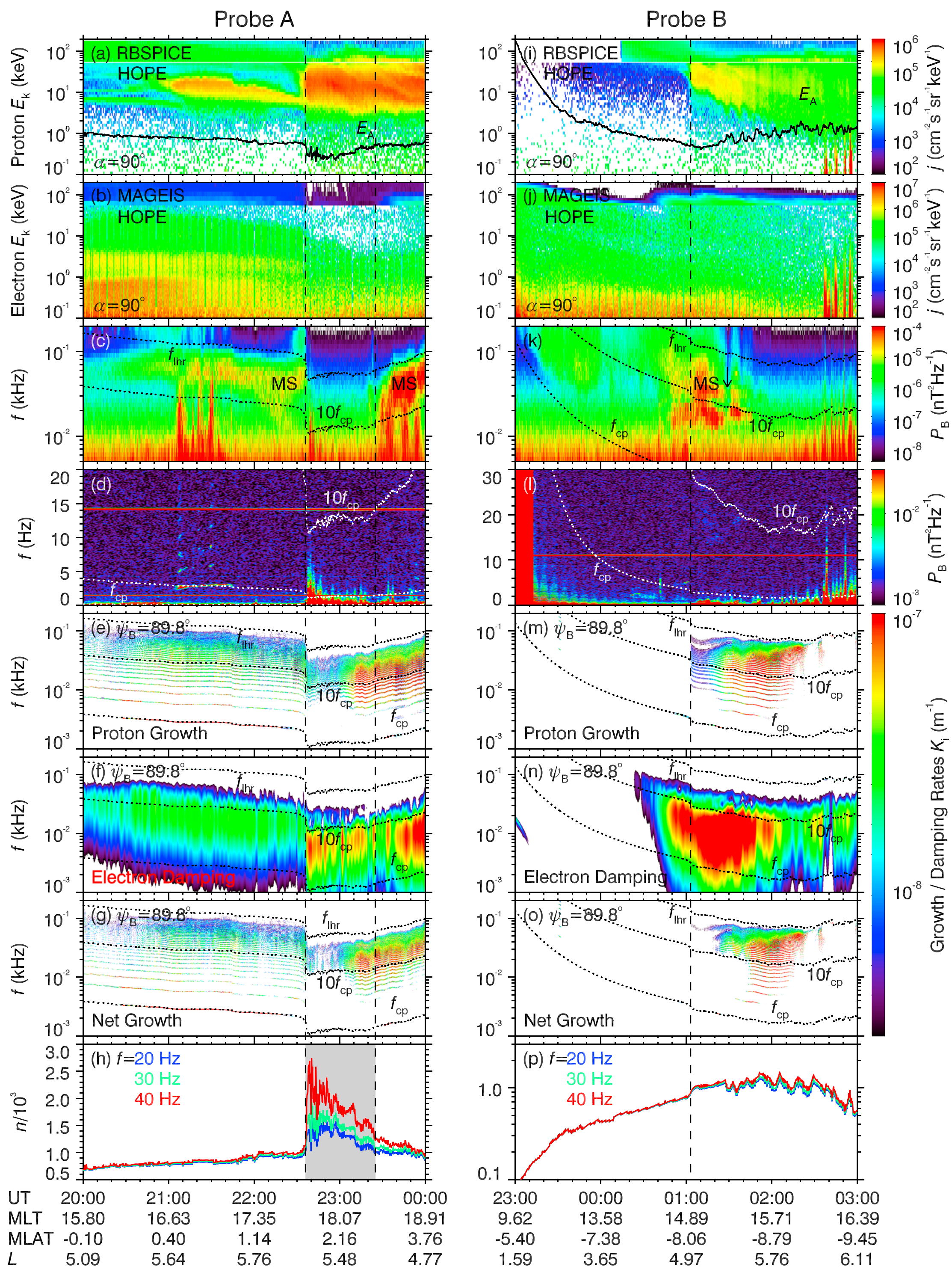

Figure 3. Generation and propagation of magnetosonic waves during 27–28 May 2017: (a and i) proton differential flux j at $\alpha = 90°$ and Alfvén energy E_A; (b and j) electron differential flux j at $\alpha = 90°$; (c and k) low-resolution wave power spectral density P_B; (d and l) high-resolution wave power spectral density P_B; (e–g and m–o) convective proton growth rate, electron damping rate, and net growth rate K_i at $\psi_B = 89.8°$; (h and p) wave refractive index n (color coded according to frequency). The vertical dashed lines in Figures 3a–3h mark the boundaries of the magnetosonic wave quenching region (gray shadow) detected by the Van Allen Probe A. The vertical dashed line in Figures 3i–3p marks the injection front detected by the Van Allen Probe B. The arrow in Figure 3k denotes the density slot without observable magnetosonic waves.

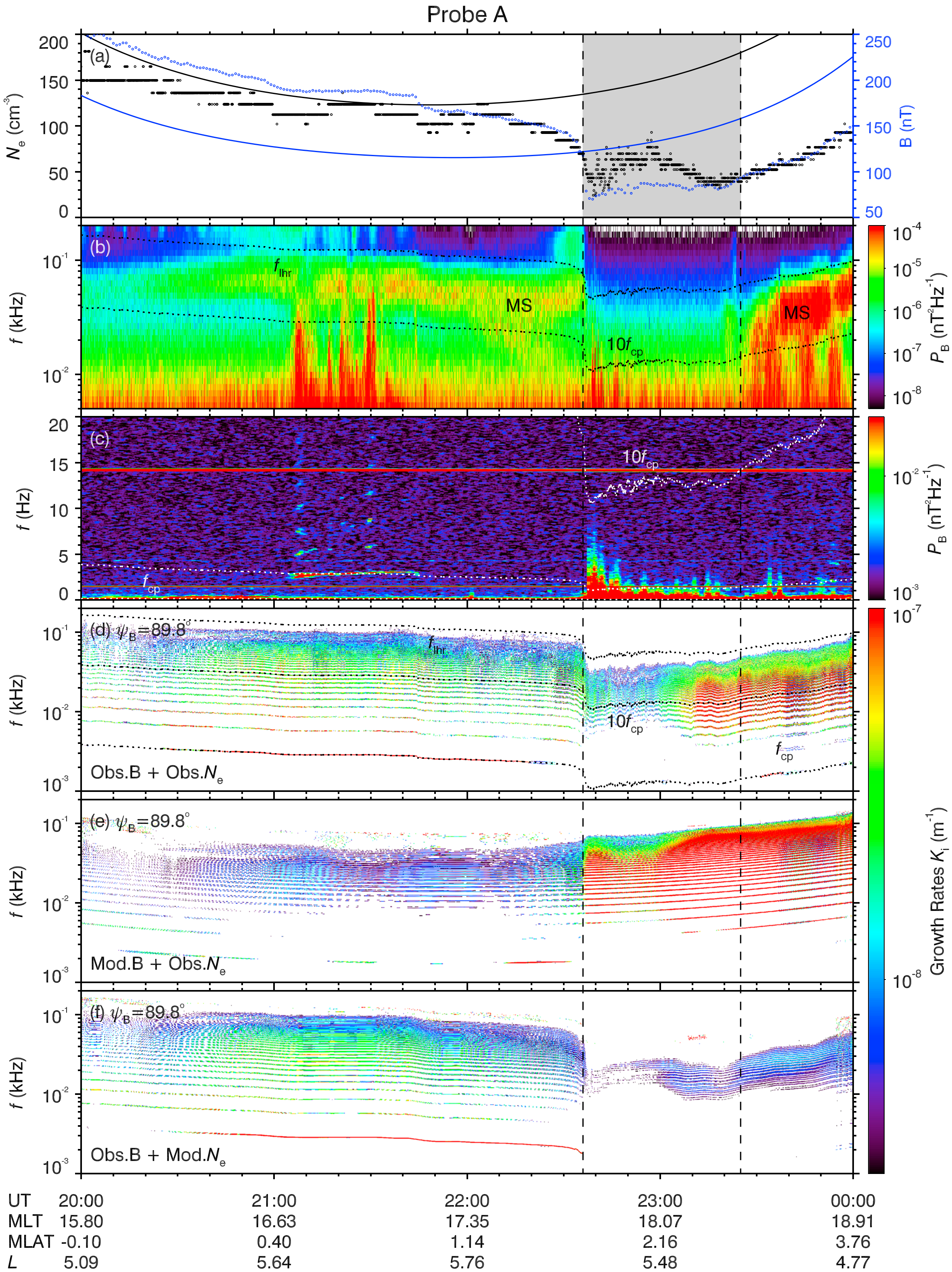

Figure 4. Sensitivity of magnetosonic growth rates to magnetic field and density parameters for the Van Allen Probe A: (a) observed (dotted) and modeled (solid) cold electron density N_e (black) and magnetic field B (blue); (b) low-resolution wave power spectral density P_B; (c) high-resolution wave power spectral density P_B; (d–f) convective growth rate K_i provided by hot protons at $\psi_B = 89.8°$ under different conditions of cold electron density and magnetic field. The vertical dashed lines in Figures 4a–4f mark the boundaries of the magnetosonic wave quenching region (gray shadow) detected by the Van Allen Probe A.

components of the wave vector, and the nth-order Bessel function J_n. The growth of waves is allowed when the weight J_n^2 is large enough at the inner edge of the proton ring where $\frac{\partial F}{\partial v_\perp} > 0$. The weight J_n^2 has a series of local maxima naturally in a descending order. The first maxima of J_n^2 occurs when $\frac{k_\perp v_\perp}{2\pi f_{\mathrm{cp}}} \approx n$. Since the magnetosonic wave has the perpendicular phase velocity $\frac{2\pi f}{k_\perp}$ close to the local Alfvén velocity V_{A}, $v_\perp = V_{\mathrm{A}}$ is roughly the first maxima location of J_n^2. In other words, the magnetosonic wave excitation is favored under the condition of V_{A} close to the inner edge of the proton ring. For the electron component, the wave damping rates (Horne et al., 2000) are controlled by the wave parallel phase velocity $\frac{2\pi f}{k_\parallel} \sim V_{\mathrm{A}} \tan \psi_{\mathrm{B}}$. The less-oblique waves under the lower V_{A} condition can resonate with the lower-energy electrons and then experience stronger Landau damping. The excited magnetosonic waves are able to propagate over a broad spatial region and experience the path-integrated amplification or attenuation (e.g., Chen & Thorne, 2012).

For the Probe A, the linear instability process with the observed magnetic field and density at the normal angle $\psi_{\mathrm{B}} = 89.8°$ can qualitatively explain the sudden quenching of the magnetosonic waves. This wave normal angle is chosen (Figure S7) to allow the dominance of the growth rates provided by hot protons over the damping rates provided by hot electrons from 21:00 to 21:45 UT. The growth rates peak at the proton gyrofrequency and decrease gradually with the frequency approaching f_{lhr}, consistent with both the high- and low-resolution wave observations. Following the substorm injection, with the Alfvén energy $E_{\mathrm{A}} = m_{\mathrm{p}} V_{\mathrm{A}}^2/2 \approx 0.3$ keV much less than the ring energy $E_{\mathrm{R}} \approx 10$ keV, the growth rates provided by hot protons decrease abruptly. (m_{p} is the proton rest mass.) Meanwhile, the V_{A} reduction causes the electron damping rates to increase to a comparable or even higher level of the growth rates related to hot protons. The decrease of the net growth rates corresponds well to the sudden quenching of waves in the low-resolution data. However, insensitive to the wave normal angle (Figure S7), the enhancement of local net growth rates appear to be 30 min earlier than the recovery of magnetosonic waves in the low-resolution data. Under the condition of $E_{\mathrm{A}} \ll E_{\mathrm{R}}$, the obtained growth rates are at a low level ($< 10^{-7}$ m^{-1}), consistent with previous calculations (Chen et al., 2010; Su et al., 2017). To become observable, these magnetosonic rays may propagate in the azimuthal direction, experience the quasi-static magnetic field, and gain energy continuously (Boardsen et al., 2018). In the medium disturbed by the substorm injection, the calculated wave refractive indices behave irregularly. The corresponding magnetosonic rays easily deviate from the path with a nearly constant magnetic field strength and gain little energy. As a result, from 22:36 to 23:24 UT with the significant fluctuations of the wave refractive indices, the magnetosonic waves were always unobservable for the Probe A. In contrast, the relatively smooth variations in the refractive indices after 23:24 UT allowed the magnetosonic waves to continuously grow to an observable level.

To test the sensitivity of the growth rates provided by hot protons to the magnetic field and density parameters, we have performed another two groups of calculations. Replacement of the observed magnetic field with the TS05-modeled magnetic field (Tsyganenko & Sitnov, 2005) causes the wave growth rates to evolve oppositely to data. The main reason is that the TS05 model underestimates the pre-injection magnetic field strength but overestimates the post-injection magnetic field strength. Replacement of the observed density with the CA92-modeled density (Carpenter & Anderson, 1992) reproduces the pre-injection wave growth characteristics but results in the quenching/weakening of magnetosonic waves in a broader frequency range over a longer time period than data. The main reason is that the CA92 model well describes the pre-injection density profile but overestimates the post-injection density by more than three times.

The magnetosonic wave quenching driven by the substorm proton injection differed from that triggered by the step change of the solar wind dynamic pressure (Liu et al., 2018b) in both the mechanism and the occurrence region. For the former, the enhanced hot proton pressure distorted the background magnetic field configuration and the cold plasma density distribution. The wave quenching likely occurred in the dusk/afternoon sector with the peak of the partial ring current. The wave quenching region could be interpreted as a zone where waves lacked sufficient gain or even became damped. Considering the drift of hot protons, we speculate that the magnetosonic wave quenching region should move toward the noonside. With the observed duration (22:36–23:24 UT) of wave quenching, the azimuthal drift velocity ~ 2 MLT/hr of hot (10–50 keV) protons, and the orbital coverage of the Probe A during the quenching period, we can estimate that the magnetosonic quenching region extended over 2 hr in magnetic local time and 0.5 R_{E} in

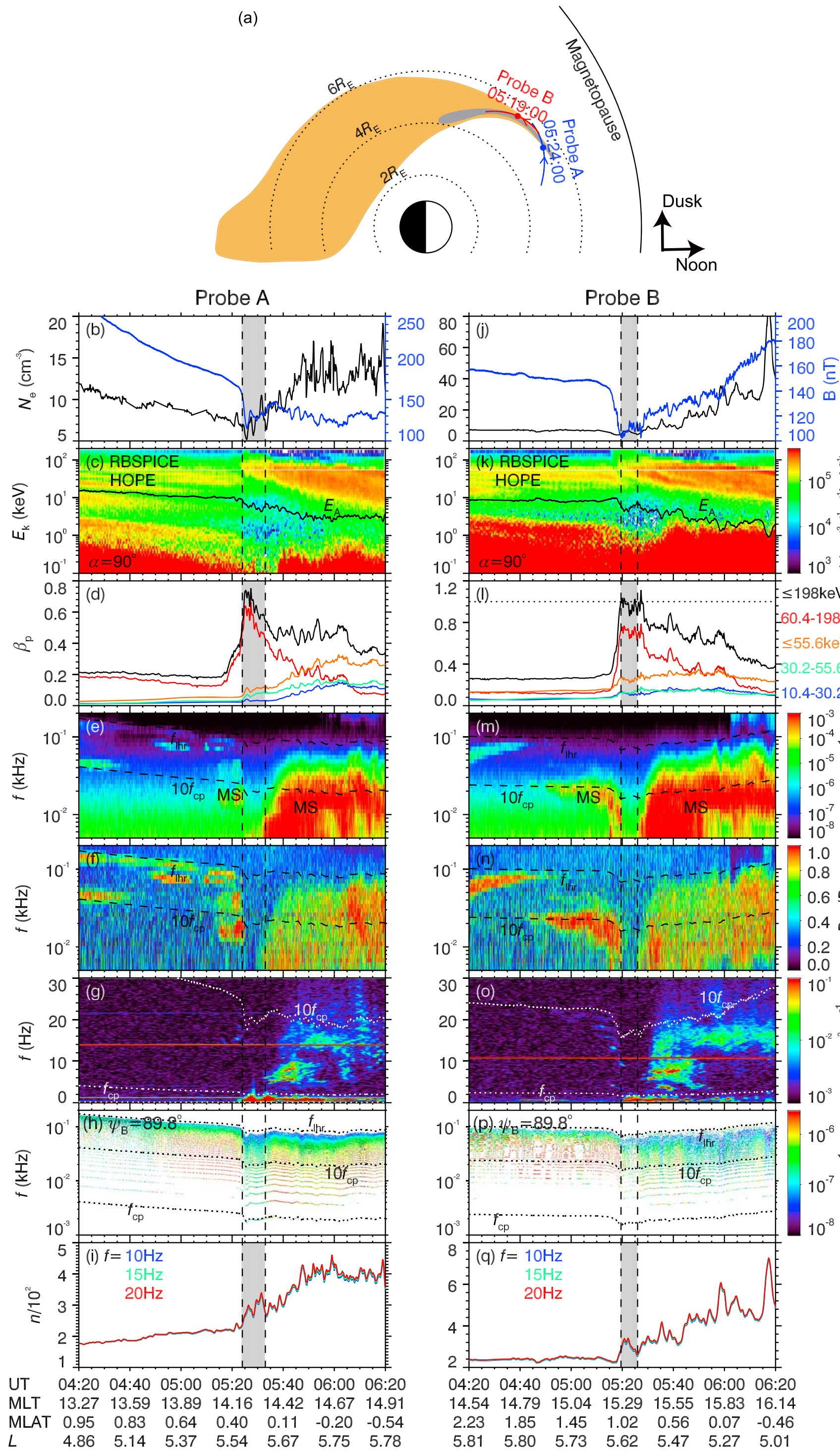

Figure 5. Overview of magnetosonic wave quenching event on 7 October 2015: (a) schematic diagrams of magnetopause (black), substorm injection region (yellow), magnetosonic quenching region (gray), and Van Allen Probes trajectories (blue for Probe A and red for Probe B); (b and j) cold electron density N_e (black) and magnetic field B (blue); (c and k) proton differential flux j at $\alpha = 90°$ and Alfvén energy E_A; (d and l) proton plasma beta β_p (color coded according to energy channel); (e and m) low-resolution magnetic wave power spectral density P_B; (f and n) magnetic compressibility $P_{B\parallel}/P_B$; (g and o) high-resolution wave power spectral density P_B; (h and p) convective growth rate K_i at $\psi_B = 89.8°$; (i and q) wave refractive index n (color coded according to frequency). The vertical dashed lines mark the boundaries of the magnetosonic wave quenching region (gray shadow) detected by the Van Allen Probes.

radial distance. (R_E is the Earth radii.) For the latter (Liu et al., 2018b), the relaxed dayside geomagnetic field caused the adiabatic deceleration of hot protons and then suppressed the local proton instability. The resulted wave quenching could be expected to occur over a broad portion of the dayside magnetosphere.

For the Probe B, the local growth rates exhibit different trends from the observed magnetosonic waves. Before and after the substorm injection, the refractive indices behave smoothly, allowing the magnetosonic wave propagation to the Probe B. There are two evidences for such a wave propagation process. One is the nearly constant frequency bands (~18 and 30 Hz, independent of the background magnetic field) of the magnetosonic waves in the low-resolution data from 00:50 to 01:45 UT. The other is the intermittence of magnetosonic waves in a density slot around 01:30 UT, which is contrary to the prediction of local instability but could be reasonably interpreted as an interruption of wave propagation by the irregular density structure.

4. Magnetosonic Wave Quenching Under Low-Density Condition

In Figure 5, we show another magnetosonic wave quenching event on 7 October 2015 to illustrate the generality of the proposed scenario. There were a multistep strong storm and the prolonged substorms (Figure S9). The apogees of the Van Allen Probes mission were located around MLT = 15. Different from the previous event, this substorm proton injection was observed under the low-density condition $N_e < 10$ cm^{-3}, by the Probe A during the outbound pass (05:24 UT, $L = 5.57$, MLT = 14.2, MLAT = 0.34°) and by the Probe B during the inbound pass (05:19 UT, $L = 5.62$, MLT = 15.3, MLAT = 1.03°). At the locations of both probes, the injection produced a trough of the magnetic field strength and the density and the quenching of magnetosonic waves, albeit lasting only for a short time (~7 min). This trough can be considered a consequence of the thermal pressure enhancement associated with the >55.6-keV proton injection. With the modeled particle distributions (Figures S10–S13), we calculate the growth/damping rates related to hot protons and electrons. Outside the trough, the peak growth rates provided by hot protons reach $\sim 2 \times 10^{-6}$ m^{-1}, allowing the substantial growth of waves even propagating within a limited azimuthal region. Inside the trough, the growth rates decrease to $\leq 2 \times 10^{-7}$ m^{-1}, corresponding to the quenching of the magnetosonic waves. As shown in Figures S14 and S15, this evolution trend of the local growth rate is robust to the specification of the different wave normal angles, and the inclusion of the Landau damping by hot electrons does not qualitatively change the results. In addition, the fluctuating refractive indices might be also unconducive to the cumulative growth of the magnetosonic waves. The two probes, separated by ~1 hr in magnetic local time, detected the quenching of magnetosonic waves within 7 min, implying that the wave quenching region extended over at least ~1 hr in magnetic local time. Within 7 min, both probes moved about 0.05 R_E along the radial direction, indicating that the radial width of the wave quenching region was about 0.05 R_E in the early afternoon sector. Considering the duskside peak of the partial ring current (e.g., Tsyganenko & Sitnov, 2005; Ukhorskiy et al., 2006) and the previous duskside observations (Figures 1–4), we speculate that, in the event on 7 October 2015, the magnetosonic wave quenching region possibly extend from early afternoon to dusk.

5. Summary

Magnetosonic waves can transfer energy from the ring current protons to the radiation belt electrons in the magnetosphere. The substorm-injected protons are traditionally expected to intensify the magnetosonic waves in the inner magnetosphere. On the basis of data collected by the Van Allen Probes, we here show that the substorm proton injections can quench the magnetosonic waves under both high- and low-density conditions. Closely following the injection front, although the proton ring distributions were strengthened, the distorted background conditions became unfavorable for the magnetosonic wave generation. The enhanced thermal pressure of protons caused the expansion of magnetic field lines and then the reduction of cold plasma density. In the newly created trough of magnetic field and density, the magnetosonic wave phase velocity was much less than the proton ring velocity, locally allowing the growth rates provided by hot protons at a low level. On the contrary, the reduction of the wave phase velocities favored the Landau damping by hot electrons particularly under the high-density condition. In addition, the spatially irregular varying refractive indices might have suppressed the cumulative growth of the magnetosonic waves along the path with a quasi-constant magnetic field. The magnetosonic wave quenching region probably drifted with the fresh protons, and for the intense injection, extended over 2 hr in magnetic local time and 0.5 R_E in radial distance. These results provide a new understanding of the generation and distribution of the magnetosonic waves during substorms.

Acknowledgments
We acknowledge EMFISIS, ECT, and RBSPICE teams for the use of Van Allen Probes data. Data are available from the following websites: http://emfisis.physics.uiowa.edu/Flight/ , http://www.rbsp-ect.lanl.gov/data_pub/ and http://cdaweb.gsfc.nasa.gov/pub/data/. This work was supported by the Key Research Program of the Chinese Academy of Sciences Grant XDPB11, the National Natural Science Foundation of China Grants 41774170, 41631071 and 41604148, the Chinese Academy of Sciences Grants KZCX2-EW-QN510 and KZZD-EW-01-4, the CAS Key Research Program of Frontier Sciences Grant QYZDB-SSW-DQC015, and the National Key Basic Research Special Foundation of China Grant 2011CB811403.

References

Balikhin, M. A., Shprits, Y. Y., Walker, S. N., Chen, L., Cornilleau-Wehrlin, N., Dandouras, I., et al. (2015). Observations of discrete harmonics emerging from equatorial noise. *Nature Communications*, *6*, 7703. https://doi.org/10.1038/ncomms8703

Blake, J. B., Carranza, P. A., Claudepierre, S. G., Clemmons, J. H., Crain, W. R., Dotan, Y., et al. (2013). The magnetic electron ion spectrometer (MagEIS) instruments aboard the radiation belt storm probes (RBSP) spacecraft. *Space Science Reviews*, *179*, 383–421. https://doi.org/10.1007/s11214-013-9991-8

Boardsen, S. A., Gallagher, D. L., Gurnett, D. A., Peterson, W. K., & Green, J. L. (1992). Funnel-shaped, low-frequency equatorial waves. *Journal of Geophysical Research*, *97*, 14. https://doi.org/10.1029/92JA00827

Boardsen, S. A., Hospodarsky, G. B., Kletzing, C. A., Engebretson, M. J., Pfaff, R. F., Wygant, J. R., et al. (2016). Survey of the frequency dependent latitudinal distribution of the fast magnetosonic wave mode from Van Allen Probes Electric and Magnetic Field Instrument and Integrated Science waveform receiver plasma wave analysis. *Journal of Geophysical Research: Space Physics*, *121*, 2902–2921. https://doi.org/10.1002/2015JA021844

Boardsen, S. A., Hospodarsky, G. B., Min, K., Averkamp, T. F., Bounds, S. R., Kletzing, C. A., & Pfaff, R. F. (2018). Determining the wave vector direction of equatorial fast magnetosonic waves. *Geophysical Research Letters*, *45*, 7951–7959. https://doi.org/10.1029/2018GL078695

Carpenter, D. L., & Anderson, R. R. (1992). An ISEE/Whistler model of equatorial electron density in the magnetosphere. *Journal of Geophysical Research*, *97*, 1097–1108. https://doi.org/10.1029/91JA01548

Chen, L., & Thorne, R. M. (2012). Perpendicular propagation of magnetosonic waves. *Geophysical Research Letters*, *39*, L14102. https://doi.org/10.1029/2012GL052485

Chen, L., Thorne, R. M., Jordanova, V. K., & Horne, R. B. (2010). Global simulation of magnetosonic wave instability in the storm time magnetosphere. *Journal of Geophysical Research*, *115*, A11222. https://doi.org/10.1029/2010JA015707

Curtis, S. A., & Wu, C. S. (1979). Gyroharmonic emissions induced by energetic ions in the equatorial plasmasphere. *Journal of Geophysical Research*, *84*, 2597–2607. https://doi.org/10.1029/JA084iA06p02597

Daglis, I. A., Thorne, R. M., Baumjohann, W., & Orsini, S. (1999). The terrestrial ring current: Origin, formation, and decay. *Reviews of Geophysics*, *37*, 407–438. https://doi.org/10.1029/1999RG900009

De Boor, C. (1977). Package for calculating with B-splines. *SIAM Journal on Numerical Analysis*, *14*(3), 441–472.

Dessler, A. J., & Karplus, R. (1961). Some effects of diamagnetic ring currents on Van Allen radiation. *Journal of Geophysical Research*, *66*, 2289–2295. https://doi.org/10.1029/JZ066i008p02289

Funsten, H. O., Skoug, R. M., Guthrie, A. A., MacDonald, E. A., Baldonado, J. R., Harper, R. W., et al. (2013). Helium, Oxygen, Proton, and Electron (HOPE) mass spectrometer for the radiation belt storm probes mission. *Space Science Reviews*, *179*, 423–484. https://doi.org/10.1007/s11214-013-9968-7

Gary, S. P., Liu, K., Winske, D., & Denton, R. E. (2010). Ion Bernstein instability in the terrestrial magnetosphere: Linear dispersion theory. *Journal of Geophysical Research*, *115*, A12209. https://doi.org/10.1029/2010JA015965

Gulelmi, A. V., Klaine, B. I., & Potapov, A. S. (1975). Excitation of magnetosonic waves with discrete spectrum in the equatorial vicinity of the plasmapause. *Planetary and Space Science*, *23*, 279–286. https://doi.org/10.1016/0032-0633(75)90133-6

Gurnett, D. A. (1976). Plasma wave interactions with energetic ions near the magnetic equator. *Journal of Geophysical Research*, *81*, 2765–2770. https://doi.org/10.1029/JA081i016p02765

He, Z., Chen, L., Zhu, H., Xia, Z., Reeves, G. D., Xiong, Y., et al. (2017). Multiple-satellite observation of magnetic dip event during the substorm on 10 october 2013. *Geophysical Research Letters*, *44*, 9167–9175. https://doi.org/10.1002/2017GL074869

Horne, R. B., Thorne, R. M., Glauert, S. A., Meredith, N. P., Pokhotelov, D., & Santolík, O. (2007). Electron acceleration in the Van Allen radiation belts by fast magnetosonic waves. *Geophysical Research Letters*, *34*, L17107. https://doi.org/10.1029/2007GL030267

Horne, R. B., Wheeler, G. V., & Alleyne, H. S. C. K. (2000). Proton and electron heating by radially propagating fast magnetosonic waves. *Journal of Geophysical Research*, *105*, 27,597–27,610. https://doi.org/10.1029/2000JA000018

Kennel, C. (1966). Low-frequency whistler mode. *Physics of Fluids*, *9*, 2190–2202. https://doi.org/10.1063/1.1761588

Kim, K. C., & Chen, L. (2016). Modeling the storm time behavior of the magnetosonic waves using solar wind parameters. *Journal of Geophysical Research: Space Physics*, *121*, 446–458. https://doi.org/10.1002/2015JA021716

Kim, K. C., & Shprits, Y. (2017). Dependence of the amplitude of magnetosonic waves on the solar wind and AE index using Van Allen Probes. *Journal of Geophysical Research: Space Physics*, *122*, 6022–6034. https://doi.org/10.1002/2017JA024094

Kletzing, C. A., Kurth, W. S., Acuna, M., MacDowall, R. J., Torbert, R. B., Averkamp, T., et al. (2013). The Electric and Magnetic Field Instrument Suite and Integrated Science (EMFISIS) on RBSP. *Space Science Reviews*, *179*, 127–181. https://doi.org/10.1007/s11214-013-9993-6

Kurth, W. S., Pascuale, S. D., Faden, J. B., Kletzing, C. A., Hospodarsky, G. B., Thaller, S., & Wygant, J. R. (2014). Electron densities inferred from plasma wave spectra obtained by the waves instrument on van allen probes. *Journal of Geophysical Research: Space Physics*, *120*, 904–914. https://doi.org/10.1002/2014JA020857

Li, J., Ni, B., Ma, Q., Xie, L., Pu, Z., Fu, S., et al. (2016). Formation of energetic electron butterfly distributions by magnetosonic waves via Landau resonance. *Geophysical Research Letters*, *43*, 3009–3016. https://doi.org/10.1002/2016GL067853

Liu, K., Gary, S. P., & Winske, D. (2011). Excitation of magnetosonic waves in the terrestrial magnetosphere: Particle-in-cell simulations. *Journal of Geophysical Research*, *116*, A07212. https://doi.org/10.1029/2010JA016372

Liu, N., Su, Z., Gao, Z., Zheng, H., Wang, Y., Wang, S., et al. (2017). Simultaneous disappearances of plasmaspheric hiss, exohiss, and chorus waves triggered by a sudden decrease in solar wind dynamic pressure. *Geophysical Research Letters*, *44*, 52–61. https://doi.org/10.1002/2016GL071987

Liu, N., Su, Z., Zheng, H., Wang, Y., & Wang, S. (2018a). Magnetosonic harmonic falling and rising frequency emissions potentially generated by nonlinear wave-wave interactions in the Van Allen radiation belts. *Geophysical Research Letters*, *45*, 7985–7995. https://doi.org/10.1029/2018GL079232

Liu, N., Su, Z., Zheng, H., Wang, Y., & Wang, S. (2018b). Prompt disappearance and emergence of radiation belt magnetosonic waves induced by solar wind dynamic pressure variations. *Geophysical Research Letters*, *45*, 585–594. https://doi.org/10.1002/2017GL076382

Ma, Q., Li, W., Chen, L., Thorne, R. M., Kletzing, C. A., Kurth, W. S., et al. (2014). The trapping of equatorial magnetosonic waves in the Earth's outer plasmasphere. *Geophysical Research Letters*, *41*, 6307–6313. https://doi.org/10.1002/2014GL061414

Ma, Q., Li, W., Thorne, R. M., & Angelopoulos, V. (2013). Global distribution of equatorial magnetosonic waves observed by THEMIS. *Geophysical Research Letters*, *40*, 1895–1901. https://doi.org/10.1002/grl.50434

Mauk, B. H., Fox, N. J., Kanekal, S. G., Kessel, R. L., Sibeck, D. G., & Ukhorskiy, A. (2013). Science objectives and rationale for the radiation belt storm probes mission. *Space Science Reviews*, *179*, 3–27. https://doi.org/10.1007/s11214-012-9908-y

Meredith, N. P., Horne, R. B., & Anderson, R. R. (2008). Survey of magnetosonic waves and proton ring distributions in the Earth's inner magnetosphere. *Journal of Geophysical Research*, *113*, A06213. https://doi.org/10.1029/2007JA012975

Min, K., Liu, K., Wang, X., Chen, L., & Denton, R. E. (2018). Fast magnetosonic waves observed by van allen probes: Testing local wave excitation mechanism. *Journal of Geophysical Research: Space Physics*, *123*, 497–512. https://doi.org/10.1002/2017JA024867

Mitchell, D. G., Lanzerotti, L. J., Kim, C. K., Stokes, M., Ho, G., Cooper, S., et al. (2013). Radiation Belt Storm Probes Ion Composition Experiment (RBSPICE). *Space Science Reviews*, *179*, 263–308. https://doi.org/10.1007/s11214-013-9965-x

Perraut, S., Roux, A., Robert, P., Gendrin, R., Sauvaud, J. A., Bosqued, J. M., et al. (1982). A systematic study of ULF waves above F_H^+ from GEOS 1 and 2 measurements and their relationships with proton ring distributions. *Journal of Geophysical Research*, *87*, 6219–6236. https://doi.org/10.1029/JA087iA08p06219

Reinsch, C. H. (1967). Smoothing by spline functions. *Numerical Mathematics*, *10*(3), 177–183.

Russell, C. T., Holzer, R. E., & Smith, E. J. (1970). OGO 3 observations of ELF noise in the magnetosphere: 2. The nature of the equatorial noise. *Journal of Geophysical Research*, *75*, 755. https://doi.org/10.1029/JA075i004p00755

Santolík, O., Parrot, M., & Lefeuvre, F. (2003). Singular value decomposition methods for wave propagation analysis. *Radio Science*, *38*(1), 1010. https://doi.org/10.1029/2000RS002523

Santolík, O., Pickett, J. S., Gurnett, D. A., Maksimovic, M., & Cornilleau-Wehrlin, N. (2002). Spatiotemporal variability and propagation of equatorial noise observed by Cluster. *Journal of Geophysical Research*, *107*, 1495. https://doi.org/10.1029/2001JA009159

Santolík, O., Pickett, J. S., Gurnett, D. A., & Storey, L. R. O. (2002). Magnetic component of narrowband ion cyclotron waves in the auroral zone. *Journal of Geophysical Research*, *107*, 1444. https://doi.org/10.1029/2001JA000146

Schmidt, G. (1979). *Physics of high temperature plasmas*. New York: Academic Press, Inc.

Sheeley, B. W., Moldwin, M. B., Rassoul, H. K., & Anderson, R. R. (2001). empirical plasmasphere and trough density model: CRRES observations. *Journal of Geophysical Research*, *106*, 25,631–25,642. https://doi.org/10.1029/2000JA000286

Shprits, Y. Y. (2009). Potential waves for pitch-angle scattering of near-equatorially mirroring energetic electrons due to the violation of the second adiabatic invariant. *Geophysical Research Letters*, *36*, L12106. https://doi.org/10.1029/2009GL038322

Shue, J., Song, P., Russell, C. T., Steinberg, J. T., Chao, J. K., Zastenker, G., et al. (1998). Magnetopause location under extreme solar wind conditions. *Journal of Geophysical Research*, *103*, 17,691–17,700. https://doi.org/10.1029/98JA01103

Spence, H. E., Reeves, G. D., Baker, D. N., Blake, J. B., Bolton, M., Bourdarie, S., et al. (2013). Science goals and overview of the Energetic Particle, Composition, and Thermal Plasma (ECT) Suite on NASAs Radiation Belt Storm Probes (RBSP) mission. *Space Science Reviews*, *179*, 311–336. https://doi.org/10.1007/s11214-013-0007-5

Su, Z., Liu, N., Zheng, H., Wang, Y., & Wang, S. (2018). Large-amplitude extremely low frequency hiss waves in plasmaspheric plumes. *Geophysical Research Letters*, *45*, 565–577. https://doi.org/10.1002/2017GL076754

Su, Z., Wang, G., Liu, N., Zheng, H., Wang, Y., & Wang, S. (2017). Direct observation of generation and propagation of magnetosonic waves following substorm injection. *Geophysical Research Letters*, *44*, 7587–7597. https://doi.org/10.1002/2017GL074362

Thomsen, M. F., Denton, M. H., Jordanova, V. K., Chen, L., & Thorne, R. M. (2011). Free energy to drive equatorial magnetosonic wave instability at geosynchronous orbit. *Journal of Geophysical Research*, *116*, A08220. https://doi.org/10.1029/2011JA016644

Tsyganenko, N. A., & Sitnov, M. I. (2005). Modeling the dynamics of the inner magnetosphere during strong geomagnetic storms. *Journal of Geophysical Research*, *110*, A03208. https://doi.org/10.1029/2004JA010798

Ukhorskiy, A. Y., Anderson, B. J., Brandt, P. C., & Tsyganenko, N. A. (2006). Storm time evolution of the outer radiation belt: Transport and losses. *Journal of Geophysical Research*, *111*, A11S03. https://doi.org/10.1029/2006JA011690

Xia, Z., Chen, L., Zheng, L., & Chan, A. A. (2017). Eigenmode analysis of compressional poloidal modes in a self-consistent magnetic field. *Journal of Geophysical Research: Space Physics*, *122*, 10. https://doi.org/10.1002/2017JA024376

Xiao, F., Yang, C., Su, Z., Zhou, Q., He, Z., He, Y., et al. (2015). Wave-driven butterfly distribution of Van Allen belt relativistic electrons. *Nature Communications*, *6*, 8590. https://doi.org/10.1038/ncomms9590

Xiong, Y., Chen, L., Xie, L., Fu, S., & Pu, Z. (2017). Relativistic electron's butterfly pitch angle distribution modulated by localized background magnetic field perturbation driven by hot ring current ions. *Geophysical Research Letters*, *44*, 4393–4400. https://doi.org/10.1002/2017GL072558

Yang, C., Su, Z., Xiao, F., Zheng, H., Wang, Y., Wang, S., et al. (2017). A positive correlation between energetic electron butterfly distributions and magnetosonic waves in the radiation belt slot region. *Geophysical Research Letters*, *44*, 3980–3990. https://doi.org/10.1002/2017GL073116